PLOS ONE

RESEARCH ARTICLE

Apparent size and morphology of bacterial microcompartments varies with technique

Nolan W. Kennedy[1], Jasmine M. Hershewe[2,3], Taylor M. Nichols[2], Eric W. Roth[4], Charlene D. Wilke[4], Carolyn E. Mills[2], Michael C. Jewett[2,3,5,6,7], Danielle Tullman-Ercek[2,7]*

1 Interdisciplinary Biological Sciences Graduate Program, Northwestern University, Evanston, Illinois, United States of America, **2** Department of Chemical and Biological Engineering, Northwestern University, Evanston, Illinois, United States of America, **3** Chemistry of Life Processes Institute, Evanston, Illinois, United States of America, **4** Northwestern University Atomic and Nanoscale Characterization Experimentation Center, Northwestern University, Evanston, Illinois, United States of America, **5** Robert H. Lurie Comprehensive Cancer Center, Northwestern University, Chicago, Illinois, United States of America, **6** Simpson Querrey Institute, Northwestern University, Chicago, Illinois, United States of America, **7** Center for Synthetic Biology, Northwestern University, Evanston, Illinois, United States of America

* ercek@northwestern.edu

Citation: Kennedy NW, Hershewe JM, Nichols TM, Roth EW, Wilke CD, Mills CE, et al. (2020) Apparent size and morphology of bacterial microcompartments varies with technique. PLoS ONE 15(3): e0226395. https://doi.org/10.1371/journal.pone.0226395

Editor: Christopher V. Rao, University of Illinois at Urbana-Champaign, UNITED STATES

Received: November 23, 2019

Accepted: February 25, 2020

Published: March 9, 2020

Data Availability Statement: All relevant data are within the manuscript and its Supporting Information files.

Funding: This work was supported by the Army Research Office (grants W911NF-16-1-0169 and W911NF-19-1-0298 to DTE). NWK and TMN received support from the National Science Foundation Graduate Research Fellowship Program (grant DGE-1842165). NWK received additional support through the National Institutes of Health Training Grant (T32GM008449) via the

Abstract

Bacterial microcompartments (MCPs) are protein-based organelles that encapsulate metabolic pathways. Metabolic engineers have recently sought to repurpose MCPs to encapsulate heterologous pathways to increase flux through pathways of interest. As MCP engineering becomes more common, standardized methods for analyzing changes to MCPs and interpreting results across studies will become increasingly important. In this study, we demonstrate that different imaging techniques yield variations in the apparent size of purified MCPs from *Salmonella enterica* serovar Typhimurium LT2, likely due to variations in sample preparation methods. We provide guidelines for preparing samples for MCP imaging and outline expected variations in apparent size and morphology between methods. With this report we aim to establish an aid for comparing results across studies.

Introduction

Scientific research has recently come under fire for what is being dubbed a crisis of reproducibility. Current studies estimate that 75–90% of findings in high-profile journals are not reproducible [1]. The issue has seeped into fields across every domain of scientific inquiry [2]. While the cause of any given irreproducible result will vary from case to case, a lack of technique standardization across studies can lead to artefactual results or false conclusions [3]. In fields in which different techniques are employed to test similar hypotheses, it is important to place results into the proper context and understand the limitations of each technique. Here, we provide guidelines for technique standardization and result interpretation in the bacterial microcompartment engineering field.

Bacterial microcompartments (MCPs) are protein-based organelles found in diverse species of bacteria [4–6]. These were originally identified in cyanobacteria and were hypothesized to

Biotechnology Training Program at Northwestern University. This project was supported in part by a fellowship award awarded to JMH through the National Defense Science and Engineering (NDSEG) Fellowship Program, sponsored by the Air Force Research Laboratory, the Office of Naval Research, and the Army Research Office. JMH received support through the Ryan Fellowship awarded by Northwestern University. MCJ and JMH also gratefully acknowledges the Air Force Research Laboratory Center of Excellence Grant FA8650-15-2-5518, the David and Lucile Packard Foundation, and the Camille Dreyfus Teacher-Scholar Program. This work made use of the BioCryo facility of Northwestern University's NUANCE Center, which has received support from the Soft and Hybrid Nanotechnology Experimental (SHyNE) Resource (NSF ECCS-1542205); the MRSEC program (NSF DMR-1720139) at the Materials Research Center; the International Institute for Nanotechnology (IIN); and the State of Illinois, through the IIN. It also made use of the CryoCluster equipment, which has received support from the MRI program (NSF DMR-1229693). These funders had no role in the study design, data collection and analysis, decision to publish, or preparation of the manuscript.

Competing interests: The authors have declared that no competing interests exist.

be viruses based on their appearance [7,8]. However, these structures were later determined to be important for the carbon concentrating mechanism for certain species of autotrophic microbes [9–12]. Since then, numerous diverse types of MCPs have been identified in species ranging from cyanobacteria and halophilic ocean-dwelling bacteria, to enteric pathogens and soil-dwelling microbes [13–15]. In addition to the cyanobacterial compartments used for carbon fixation, many MCPs are used by enteric pathogens for the metabolism of unique carbon sources that move through toxic or volatile intermediates, imparting a competitive advantage [16–19].

The flagship archetype for metabolic MCPs is the 1,2-propanediol utilization (Pdu) MCP found in *Salmonella enterica*. The Pdu MCP encapsulates the enzymatic machinery necessary for metabolism of 1,2-propanediol (1,2-PD), a carbon source found in the gut of *Salmonella* hosts [16]. The 1,2-PD metabolic enzymes are surrounded by a protein shell composed of multiple types of trimeric, pentameric, and hexameric shell proteins. The reported size of these irregularly-shaped protein organelles varies widely from 77–220 nm in diameter (S1 Table), and rigorous methods for size quantification are sparse [8,13,16,20–24].

The Pdu MCP has been studied in-depth since the early 1990s, but it has recently increased in popularity due to its potential utility in metabolic engineering [25–27]. Metabolic engineers have sought to increase flux through target pathways of interest by increasing local concentrations of enzymes and their substrates [28]. MCPs can accomplish this task and offer the potential added benefit of sequestering toxic or volatile intermediates from damaging or escaping the cell [29,30]. They also have the potential to reduce unwanted side reactions and provide private cofactor pools separate from central metabolism [31].

Recent efforts to engineer MCPs focused on loading heterologous proteins to the lumen of these structures, as well as modifying the MCP shell to alter substrate and product diffusion [24,32]. Even modest engineering efforts can affect the size, shape, and morphology of MCPs. For example, knocking out or over-expressing different shell proteins leads to dramatic changes in the shape of MCPs, with many appearing to be long, hollow tubes [33–37]. As engineering efforts continue, it will become increasingly important to have a standardized set of tools for the field to determine and compare the size, shape, and morphology of engineered or altered MCPs across different studies. To date, there is no widely agreed-upon method for visualizing and measuring MCPs, with labs across the field utilizing their own preferred technique. Here we demonstrate that different techniques can yield variable apparent results, even on identical samples. We provide an outline for choosing an appropriate technique and subsequently correlate the results across the many visualization and sizing techniques used in the field.

Methods

Microcompartment expression and purification

Intact Pdu MCPs were purified from lysed cultures of *Salmonella enterica* serovar Typhimurium LT2 using a centrifugation process as previously described [38–40]. Briefly, starter cultures were grown in 5 mL of LB-Miller for 24 hours at 30˚C, 225 RPM and subsequently subcultured 1:1000 into 200 mL of no carbon-E (NCE) minimal media (29 mM KH_2PO_4, 34 mM K_2HPO_4, 17 mM $Na(NH_4)HPO_4$, 1 mM $MgSO_4$, and 50 μM ferric citrate) supplemented with 42 mM succinate as a carbon source and 55 mM 1,2-propanediol for MCP induction. NCE cultures were grown at 37˚C, 225 RPM to a final target OD_{600} of ~1–1.5, after which they were harvested and lysed. Cells were lysed chemically as previously described using a 1% (w/v) octyl thioglucoside solution in 20 mM Tris (pH 7.5) [38–40]. The lysed cultures were centrifuged at 12,000 x G for 5 minutes to remove cell debris. MCPs were then pelleted from the

resulting supernatant through centrifugation at 21,000 x G for 20 minutes and collected. The total protein concentration of MCP samples was measured using the Pierce™ BCA Protein Assay Kit (Thermo Scientific) per the manufacturer's instructions, and concentrations were normalized as necessary for each analysis method. All MCP samples were stored at 4˚C until use and were prepared for analysis within 5 days of purification to avoid MCP aggregation and degradation [41]. The same three biological replicates were used for negative-stain transmission electron microscopy (TEM), TEM with hexamethyldisilazane (HMDS), and scanning electron microscopy (SEM) analyses. Another batch of three biological replicates was used for analysis by cryo-TEM and TEM of ultra-thin sections. A final batch of three biological replicates was used for analysis via dynamic light scattering (DLS).

Protein electrophoresis

Purified MCPs were assessed for composition by SDS-PAGE as previously described [39]. Briefly, MCP samples were boiled in Laemmli buffer at 95˚C for 5–7 minutes. The denatured samples were then loaded onto 15% SDS-PAGE gels and separated at 120 V for 90 minutes. Approximately 2–2.25 μg total protein was loaded for each sample, as measured by BCA assay. Gels were then stained with Coomassie and imaged using the Bio-Rad ChemiDoc XRS+ (S1 Fig).

Negative-stain transmission electron microscopy

Samples were set on 400 mesh Formvar-coated copper grids (EMS Cat# FF400-Cu) with a carbon film. Grids were treated by glow discharge using a PELCO easiGlow glow discharge cleaning system for a total of 10 seconds at 15 mA. MCP samples were placed onto the grids immediately following glow discharge. We found that staining and contrast were best if MCPs were left undiluted (between 0.5–1.0 mg/mL). A volume of 10 μL of purified MCPs was pipetted onto the surface of the grids, which were held in place by negative-action tweezers. The samples were allowed to sit for 2 minutes before being wicked away with filter paper. Note that some of the liquid should always be left on the grid to avoid sample collapse. The samples were washed three times by dipping the grid in a small droplet of deionized water for three seconds. The samples were fixed by placing 10 μL of 2% (v/v) glutaraldehyde onto the grid for 2 minutes. Note that glutaraldehyde should be stored under N_2, and the 2% dilution should be made fresh before each sample preparation session. After the 2-minute incubation, the glutaraldehyde was wicked away using filter paper and the sample was washed three times in deionized water. Samples were stained with 1% (w/v) aqueous uranyl acetate (UA) by applying 10 μL of UA to the grids for 2 minutes. The UA was wicked away completely using filter paper. Note that all samples, fixative, stain, and deionized water were spun at 12,000 x G for 2 minutes before use to remove any aggregates. Samples were imaged at the Northwestern Electron Probe Instrumentation Center (EPIC) using the Hitachi HT-7700 Biological S/TEM Microscope and the Galtan Orius 4k x 2.67k digital camera.

For samples that were exchanged into solvent to prevent collapsing, samples were first fixed as described above in 2% glutaraldehyde. The samples were exchanged into 30% (v/v) ethanol for 1 minute, then 50% (v/v), 70% (v/v), and 90% (v/v) ethanol, followed by 100% ethanol three times. After this exchange into ethanol, samples were exchanged into 50% (v/v) and then 100% hexamethyldisilazane (HMDS). Samples exchanged into 100% HMDS were stained with UA as described above.

Scanning electron microscopy

Samples were spotted and fixed onto 400 mesh Formvar-coated copper grids (EMS Cat# FF400-Cu) and processed through a 100% ethanol exchange as described above. Grids were

placed into a sample holder and loaded into a Tousimis critical point dryer. The critical point dryer was run for a 10-minute purge cycle. Grids were mounted onto SEM stubs with carbon tape and coated with 6 nm of gold/palladium in a Cressington 208H sputter coater. Grids were imaged using a Hitachi SEM with 2 kV accelerating voltage and a 4 mm working distance.

Cryo transmission electron microscopy

Lacey Carbon 200 mesh Cu grids (EMS Cat# LC200-CU) were glow discharged in a Pelco easi-Glow glow discharger for 30 seconds at 30 mA. 4 μL of sample solution was carefully pipetted onto the grids and plunge frozen in liquid ethane in a FEI Vitrobot Mark III with a blotting time of 5 seconds and blot offset of 0.5 mm. Grids were stored in liquid nitrogen and loaded into a Gatan 626.6 Cryo Transfer Holder cooled down to -170˚C prior to observation in a JEOL JEM-1230 LaB6 emission TEM running at 100 kV. Images were collected with a Gatan Orius SC1000 CCD Camera, Model 831.

Transmission electron microscopy of ultra-thin sections

Samples were pelleted at 21,000 x G in an Eppendorf 5424 microcentrifuge for 10 minutes. Pelleted samples were fixed with 2.5% (v/v) glutaraldehyde and 2% (v/v) paraformaldehyde in 0.1M PBS, post-fixed with 1% (w/v) OsO4 and 1% (w/v) UA, dehydrated in a graded series of ethanol, infiltrated with EMBed 812 epoxy resin, and embedded in beam capsules. The embedded samples were polymerized at 60˚C for 48 hours prior to ultra-thin sectioning utilizing a Leica UC7 ultramicrotome. Sections were collected on 150 mesh Cu grids with a formvar/carbon membrane and stained with 3% (w/v) UA in 50% (v/v) methanol and Reynold's lead citrate to further enhance contrast. The samples were observed in a JEOL JEM-1230 LaB6 emission TEM at 100 kV. Images were collected with a Gatan Orius SC1000 CCD Camera, Model 831.

Dynamic light scattering measurements

Samples were centrifuged at 12,000 x G for 5 minutes at 4˚C immediately before dynamic light scattering (DLS) analysis to remove aggregated or insoluble protein. Dynamic light scattering was performed on a Zetasizer Nano ZS (Malvern Instruments Ltd., UK) with a measurement angle of 173˚. Measurements were collected in triplicate at 4˚C for 13 scans per measurement. Refractive index and temperature-adjusted viscosity were obtained from the instrument's parameter library.

Nanoparticle tracking analysis was performed on a Nanosight NS300 using a 488 nm (blue) laser (Malvern Instruments Ltd., UK). Instrument settings were adjusted according to manufacturer recommendations. Measurements were collected for a duration of 60 s in 5 runs using a 1 mL syringe and a syringe pump speed of 30. Measurements were collected at room temperature.

Image analysis and sizing

Images were contrast-adjusted and cropped using ImageJ [42]. For MCP sizing, images were scale-corrected based on the instrument used to collect the images. The oval tool was used to manually trace an ellipse surrounding MCPs. The longest diameter in the ellipse, corresponding to the widest diameter for the MCP, was recorded. Further data analysis was carried out using Microsoft Excel or R. A single-factor ANOVA was performed to determine if populations were significantly different. Two-tailed t-tests were used to determine significance of differences between specific populations.

Results and discussion

Negative-stain TEM of purified MCPs yields MCPs that appear deflated

Imaging MCPs using negative-stain transmission electron microscopy (TEM) is a standard technique used by the MCP field that has been widely adopted since Sinha and colleagues first described a method for MCP purification [40]. This technique enables clear identification of the border of each MCP, facilitating descriptions of shape and morphology (Table 1). Additionally, these results are generally higher contrast than techniques that involve imaging unpurified MCPs, such as TEM of ultra-thin cell sections.

A drawback to the negative-stain TEM technique is that it requires sample dehydration as part of the sample preparation process. This ultimately leads to MCP collapse or deflation, as indicated in Fig 1A. Dark staining is present at the MCP interior, indicating that the stain is

Table 1. Comparison of different techniques used for MCP analysis.

Method	Strengths	Weaknesses	Specialized Equipment	Previous Works
Transmission Electron Microscopy (TEM)	•Relatively simple instrumentation, compared to other techniques •Sample preparation is fast and straightforward •Easy to see surface and shape morphology •History of use in the field	•Compartments appear collapsed due to sample preparation methods •Size analysis is slow compared to DLS, etc.	•Glow Discharge System •Transmission Electron Microscope	[21,23–25,31,33,38,41,43–54]
Ultra-thin section Transmission Election Microscopy (TEM)	•Can visualize compartments in native context (does not require purification) •History of use in the field	•Relatively slow and difficult sample preparation, requiring multiple pieces of specialized equipment •Cannot readily visualize surface morphology •*In vivo* images are difficult to analyze due to other cellular components •Due to the irregular shape of compartments, size determination using this method yields a wide distribution of apparent compartment diameters, skewing results	•Ultramicrotome •Transmission Electron Microscope	[8,16,17,20,23,25,31,34–37,41,43–46,52,55–57]
Scanning Electron Microscopy (SEM)	•Compartments appear more true-to-size (less collapsed) •Can visualize surface and shape morphology	•Compartments appear slightly collapsed •Staining with a metal coat can hide surface morphologies and alter apparent size •Sample preparation and imaging is relatively complex and requires multiple pieces of specialized equipment	•Glow Discharge System •Critical Point Dryer •Sputter Coater •Scanning Electron Microscope	
Transmission Electron Cryo-microscopy (Cryo TEM)	•Compartments retain solution size, shape, and morphology the best	•Sample preparation and imaging is difficult •Contrast is low due to lack of staining	•Glow Discharge System •Plunge freezer •Cryo transfer holder •Transmission electron microscope	[22,58]
Dynamic Light Scattering (DLS), etc.	•The most rapid, high-throughput method for determining the size distribution of a population of compartments	•Does not provide information on morphology	•DLS, Zeta Sizer, other system	[41,48,52]

Table 1 lists the various techniques, along with their strengths and weakness, that are utilized in the MCP field and are assessed in this work. We have also included a brief list of specialized equipment necessary for each technique, and a list of previous works in the MCP field in which each technique was used. Our hope is that this will enable selection of the technique best-suited for each study.

https://doi.org/10.1371/journal.pone.0226395.t001

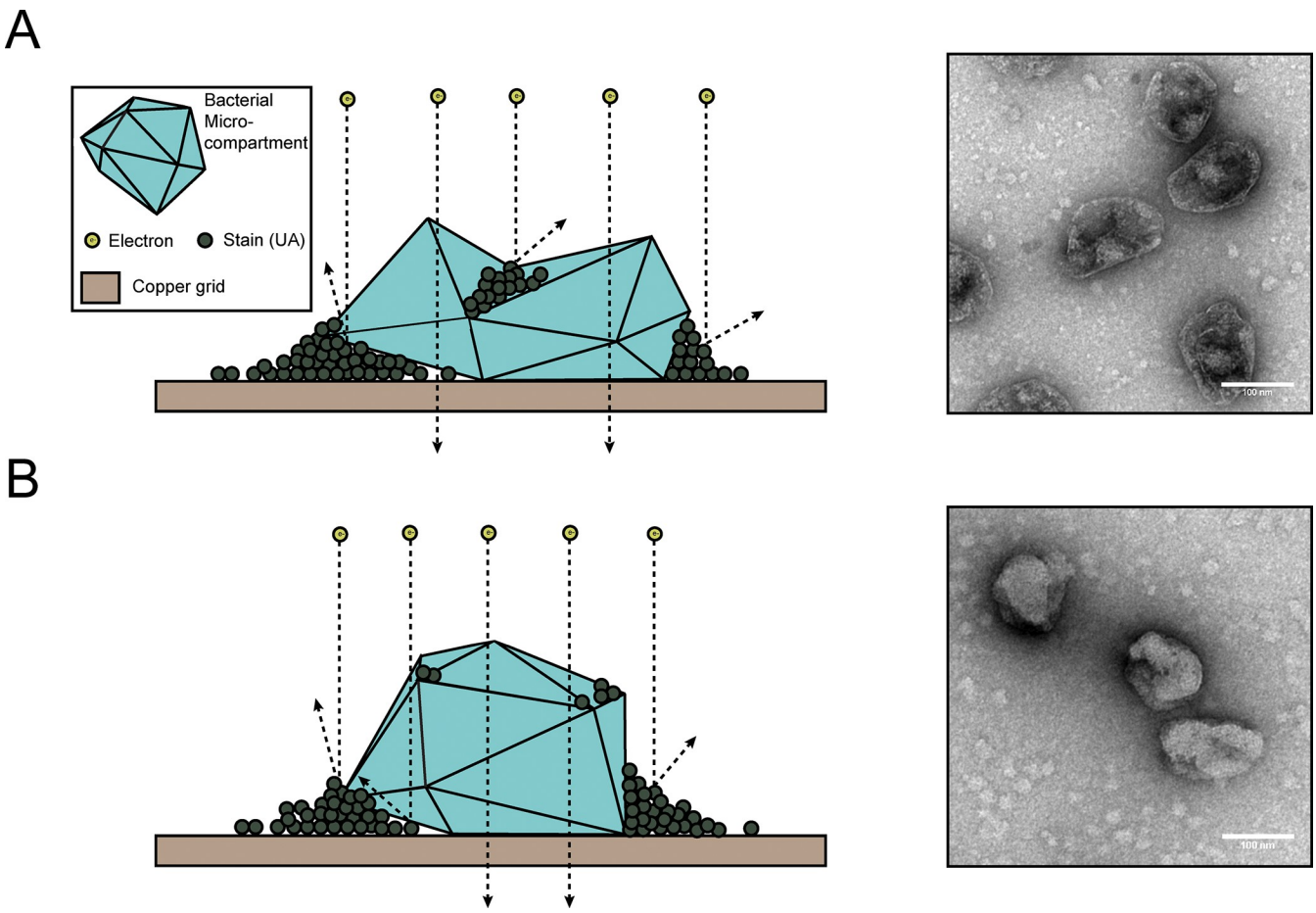

Fig 1. TEM of purified MCPs. (A) Schematic representation and transmission electron micrograph of negatively stained purified MCPs. Note that MCPs appear collapsed as evidenced by the pooled stain near the center of MCPs. (B) Schematic representation and transmission electron micrograph of negatively stained purified MCPs that were first dehydrated in ethanol and a high vapor-pressure solvent (HMDS). Note that MCPs appear less collapsed than in (A). Scale bar (white) is 100 nm.

https://doi.org/10.1371/journal.pone.0226395.g001

pooling in the collapsed, cup-shaped MCPs. To avoid this, fixing with glutaraldehyde is often used, but does not seem to completely prevent MCP collapse. MCPs appeared to be 102 ± 17 nm (mean ± standard deviation) in diameter when measured in images generated with this method (Fig 2).

We attempted a number of alterations to the standard sample preparation technique to reduce MCP collapse. This included critical point drying and sample buffer exchange from the aqueous sample buffer into a high vapor-pressure solvent. These methods improved MCP structure retention, especially in samples that were exchanged into the high vapor-pressure solvent hexamethyldisilazane (HMDS) (Fig 1B). Overall this sample preparation technique increased the average apparent diameter of the MCPs by 22% to 124 ± 17 nm and required minimal additional steps (less than an hour of additional preparation time, even with multiple samples) (Fig 2). However, the exchange into HMDS led to inconsistent staining across the sample grid. This is likely due to the minimal miscibility of HMDS and the aqueous UA stain. In spite of these inconsistencies, this technique may be useful when attempting to estimate the approximate diameter of engineered MCPs using negative-stain TEM.

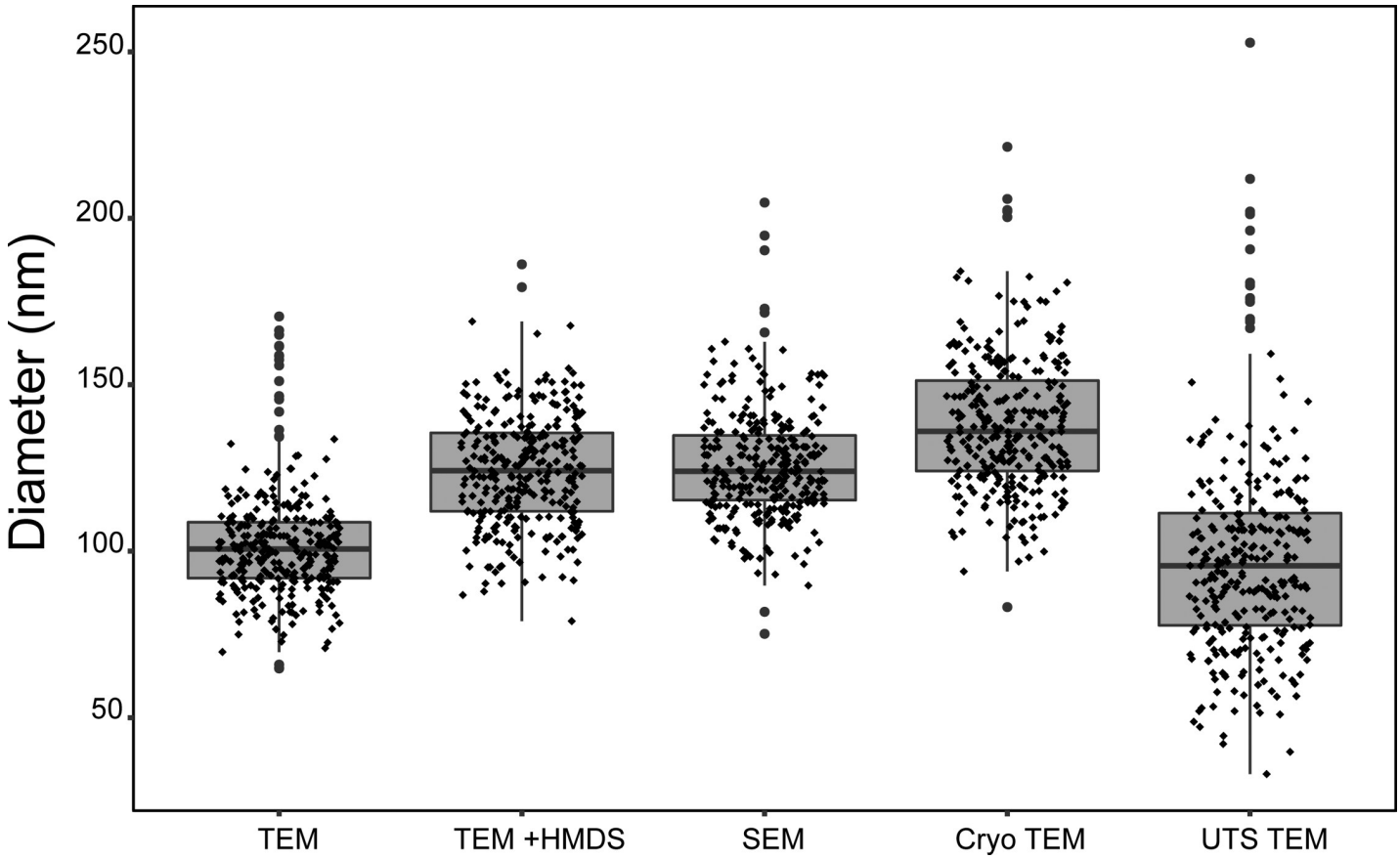

Fig 2. Apparent size of MCPs analyzed with different imaging techniques. Box-and-whisker plot of the size distribution of MCPs analyzed with various techniques. Note that apparent size and distribution varies widely with each technique. A single-factor ANOVA test revealed that populations differed significantly ($p < 0.001$). The only populations that are not significantly different (as defined by a p-value greater than .001 in a two-tailed t-test) are TEM of purified MCPs vs thin section TEM and SEM of purified MCPs vs TEM of dehydrated samples (p = .12 and .26, respectively). N = 300 for all, where 100 measurements were made for each of three biological replicates (three different MCP growths and purifications). Abbreviations: transmission electron microscopy (TEM), transmission electron microscopy with samples dehydrated in hexamethyldisilazane (TEM + HMDS), scanning electron microscopy (SEM), cryo transmission electron microscopy (Cryo TEM), ultra-thin section transmission electron microscopy (UTS TEM).

https://doi.org/10.1371/journal.pone.0226395.g002

Critical point drying and scanning electron microscopy reduces apparent MCP collapse

A technique that has not been widely adopted in the MCP field is scanning electron microscopy (SEM) (Table 1). This technique utilizes critical point drying to retain the structure of imaged samples. This is followed by treating with a sputter coater, which coats the sample in a thin layer of metal. In contrast to negative-stain TEM sample preparation, this method does not utilize an aqueous stain. For this reason, we hypothesized that critical point drying and SEM would lead to MCPs that appeared more inflated. Indeed, MCPs that were subjected to this sample preparation and imaging workflow did appear slightly more inflated than either of the negative-stain TEM methods described above (Fig 3). Coating for SEM also allows for tuning of the coat thickness, though there is an upper limit as increasing the metal coating thickness hindered detection of surface morphology (Fig 3B and 3C). For example, in Fig 3B, a coat thickness of >6 nm was used and occluded some morphological features visible in Fig 3C, which had a coat thickness of 6 nm. For this reason, we recommend using a minimal coat thickness (6 nm) (Fig 3C), although finding a balance between optimal coat thickness, accelerating voltage, and scan speed will be necessary for each case. Overall, this technique yielded

MCPs that appeared 24% (126 ± 17 nm diameter) larger, on average, than the standard negative-stain TEM method widely adopted by the field and allowed for visualization of MCP surface morphology comparable to the detail seen with negative-stain TEM (Fig 2). However, the additional sample preparation steps and specialized equipment may make this technique less appealing for many applications. Specifically, SEM sample preparation and imaging time per sample were approximately double that of TEM.

Cryo transmission electron microscopy maintains inflated MCPs

Recently, cryogenic transmission electron microscopy (cryo TEM) was used to determine the structure of an intact MCP from *Haliangium ochraceum* [58]. This MCP is unique in that it is relatively small (6.5 MDa, as opposed to the 600 MDa Pdu MCP), regular in shape, lacks natively-encapsulated enzyme cargo, and was reconstructed heterologously [58,59]. We hypothesized that because cryo TEM keeps the sample in vitreous ice and does not remove the sample from its native buffer, it would be best suited for retaining fully-inflated MCPs in their native shape and diameter (Fig 4). Indeed, samples that were imaged using cryo TEM produced images that on average appeared the largest of any of the techniques we attempted (138 ± 21 nm diameter). These MCPs appeared 35% larger in diameter than the standard negative-stain TEM technique and 10% larger than SEM. Samples imaged using cryo TEM also had similar variation in size observed by the other techniques, indicating that the higher average size is not due to large outliers (Fig 2). Indeed, cryo TEM had the second fewest outliers of any of the imaging techniques we used to assess the population size distribution.

While cryo TEM retained inflated MCPs, the lack of any contrast agent makes visualizing surface features nearly impossible. Additionally, the initial technical training for sample preparation and imaging using cryo TEM is challenging. However, an experienced microscopist can acquire cryo TEM data routinely in a single day. By contrast, chemical processing for TEM of ultra-thin sections can take several days and includes extra steps such as ultramicrotomy. Therefore, since this technique retains the native, uncollapsed state of MCPs, labs may choose to use this technique if a study is primarily focused on a change in MCP size or shape, especially on a limited number of samples (Table 1).

Ultra-thin section transmission electron microscopy yields large variation in apparent size

Besides negative-stain TEM of purified MCPs, the technique most widely used in the field is TEM of ultra-thin sections. This technique has been used both on purified MCPs as well as

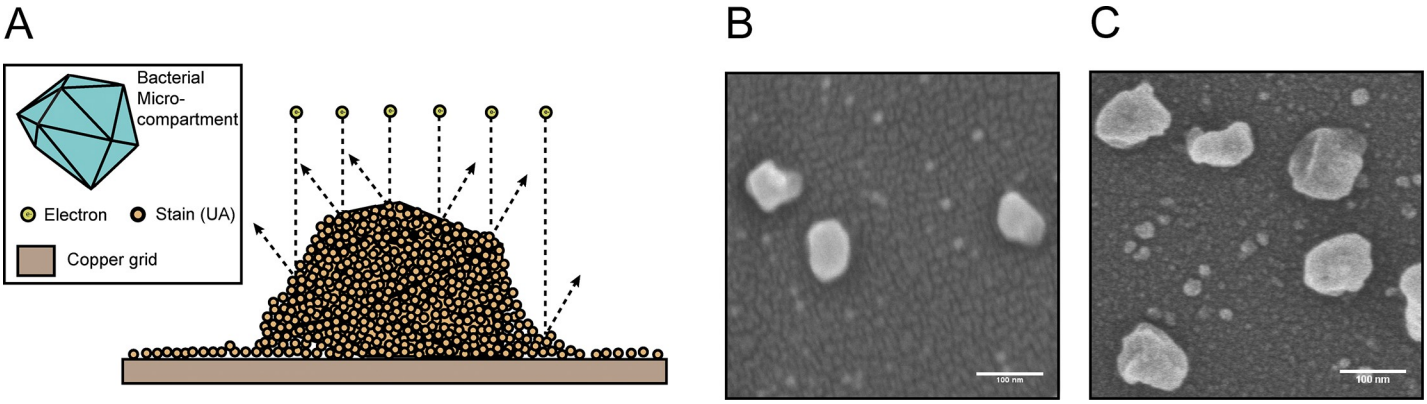

Fig 3. SEM of purified MCPs. (A) Schematic representation of MCPs imaged by SEM. (B) SEM of MCPs with >6 nm of gold staining. (C) SEM of MCPs with the minimal 6 nm gold coat thickness. Note that MCPs appear more inflated than in Fig 1A and surface features are apparent. Scale bars (white) are 100 nm.

https://doi.org/10.1371/journal.pone.0226395.g003

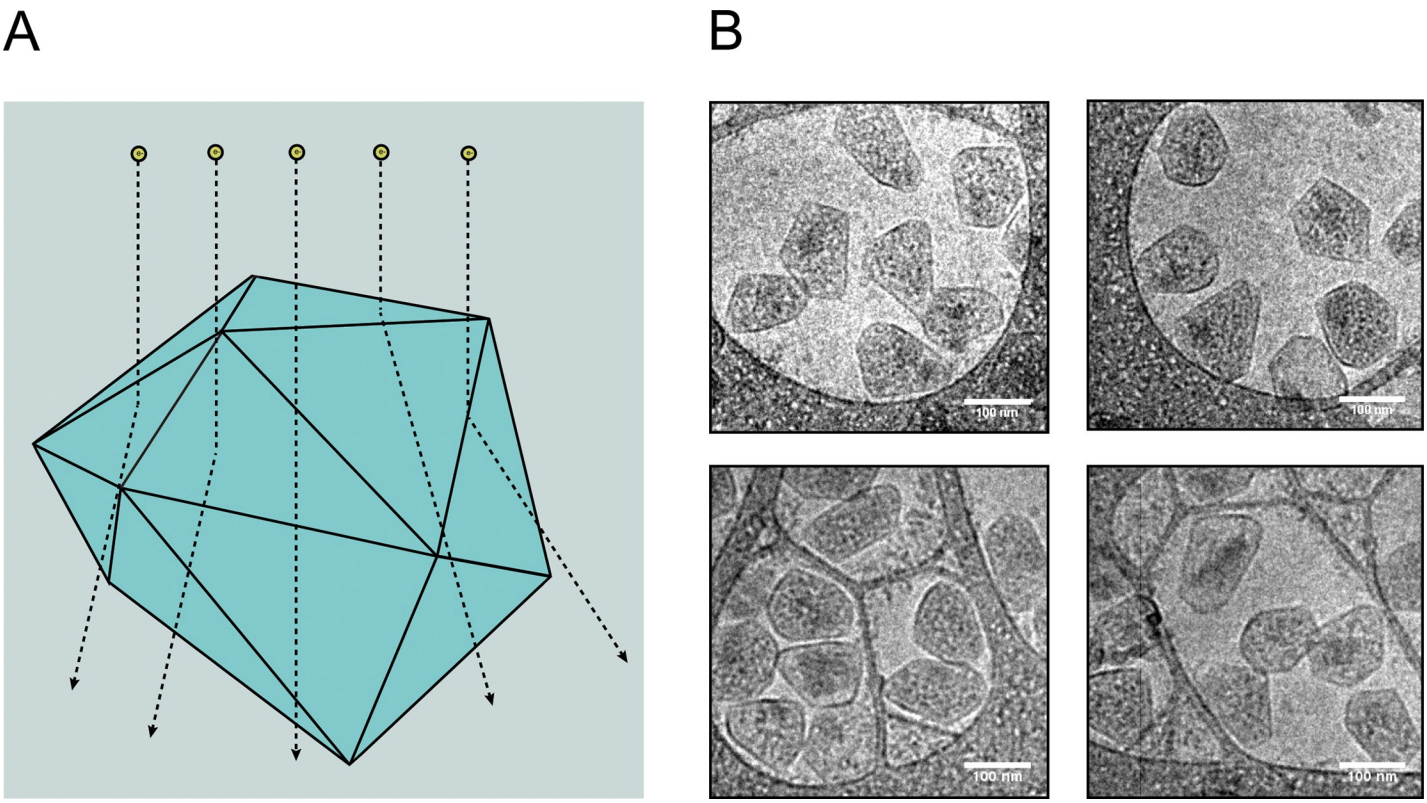

Fig 4. Cryo TEM of purified MCPs. (A) Schematic representation of cryo TEM of MCPs. Note that MCPs retain their native shape and are frozen in a layer of vitreous ice. (B) Micrographs of purified MCPs visualized using cryo TEM. Scale bars (white) are 100 nm.

https://doi.org/10.1371/journal.pone.0226395.g004

MCPs in cells. In the earliest studies in the field, this technique was the only available option for visualizing MCPs, as a purification method was not published until relatively recently (carboxysomes were discovered in 1956 but the method for Pdu MCP purification was not published until 2012) [7,40]. This allowed for visualization of MCPs within their native context and provided researchers with a means to determine if genetic manipulations altered the expression, size, shape, and cytoplasmic distribution of MCPs.

However, TEM of ultra-thin sections has a number of drawbacks that make it a suboptimal choice for many applications. Ultra-thin sections produce highly variable apparent diameters (99 ± 32 nm) likely because Pdu MCPs are irregular in shape and because measured MCP diameter depends where the MCP is sectioned (Fig 5). We illustrate the impact of this second point by assuming a spherical MCP with volume V_{sphere}. We can calculate the average diameter measured, D_{measured}, by ultra-thin sectioning using the following equation

$$D_{\text{measured}} = \frac{1}{V_{\text{sphere}}} \int_V d(r)\, dV$$

where $d(r)$ is the diameter of a spherical cross-section taken at an arbitrary radius, r, from the center of the sphere (S2 Fig). Evaluating this integral over the entire sphere volume (see S2 File), we find that the average diameter measured by ultra-thin sectioning of a sphere is related to the actual sphere diameter, D_{actual} by the equation

$$D_{\text{measured}} = \frac{3\pi}{16} D_{\text{actual}}$$

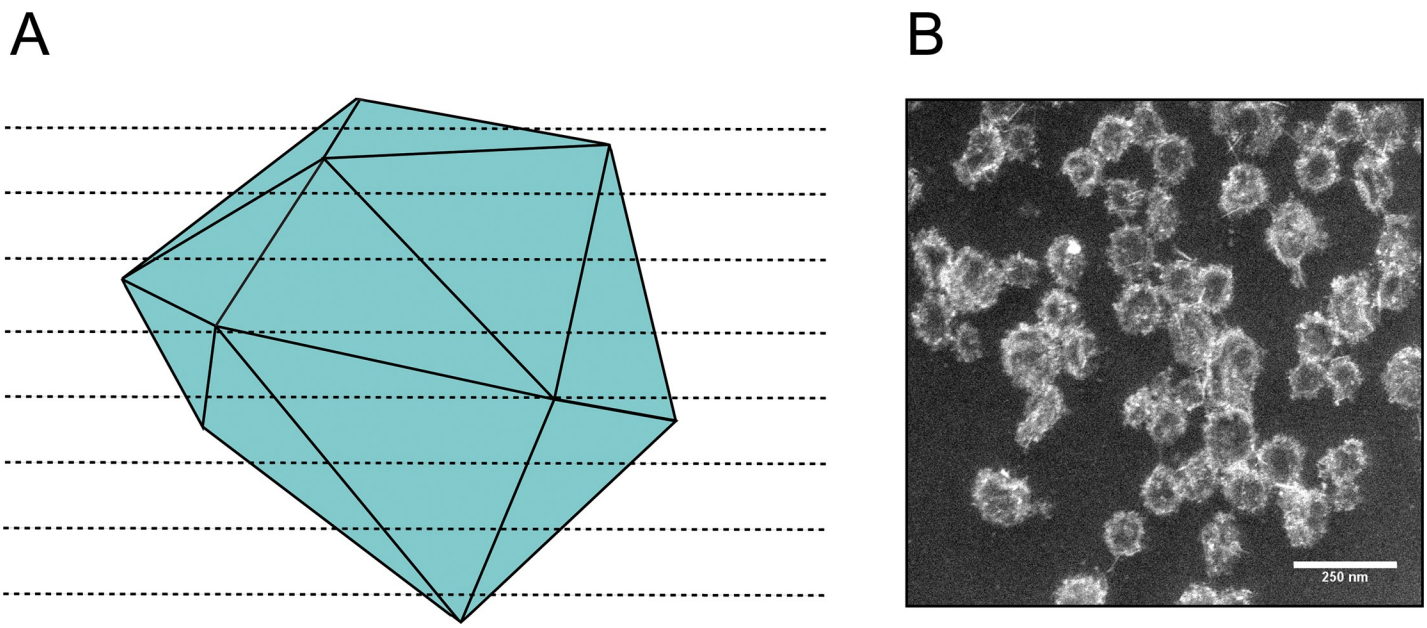

Fig 5. TEM of ultra-thin sections of purified MCPs. (A) Schematic representation of an MCP undergoing ultra-thin sectioning. Note that due to the irregular shape of MCPs, thin sectioning will lead to a wide range of apparent diameters. (B) Micrographs of purified and ultra-thin sectioned MCPs. Scale bar (white) is 250 nm.

https://doi.org/10.1371/journal.pone.0226395.g005

Thus, even if the MCPs were perfectly spherical, we expect that TEM of ultra-thin sections would underestimate the true diameter by approximately 41%. This underestimation, compounded with the irregular shape of actual Pdu MCPs, likely leads to the high variability we observed in MCP diameter measured by TEM of ultra-thin sections. Using this technique, we found the largest variation in apparent MCP diameter, with measurements both much larger and much smaller than all previous techniques (Fig 5). Indeed, MCPs appeared on average 28% smaller in diameter than with cryo TEM, and the variation was between 1.5 and 1.9 times greater than all other methods (Fig 2). While the observed 28% underestimation is less than the mathematically predicated 41% underestimation, we attribute this to difficulty in identifying the smallest MCP sections during image analysis. Qualitatively, MCPs visualized using TEM of ultra-thin sections appeared more rounded and less angular than with other techniques. However, this is not always the case across the field, as other labs have used this technique to produce MCP images that appear to retain their native angularity [8].

Additionally, preparation of ultra-thin sections is a challenging technique to master, and it can be difficult to determine the true boundaries of MCPs when they are visualized within cells. Due to these many drawbacks, we recommend only using TEM of ultra-thin sections when it is necessary to view MCPs in their native context in the cytoplasm or when it is necessary to image the interior of MCPs (Table 1).

Dynamic light scattering and nanoparticle tracking analysis enables higher-throughput MCP sizing

While microscopy allows researchers to visualize the morphology of MCPs, this may not be necessary for all studies. These imaging techniques are relatively low-throughput, and size determination is slow. One higher-throughput option for MCP sizing is particle sizing via dynamic light scattering (DLS). In this study we compared two different DLS-based techniques—Nanosight for nanoparticle tracking analysis (NTA), and Zeta Sizer for population-

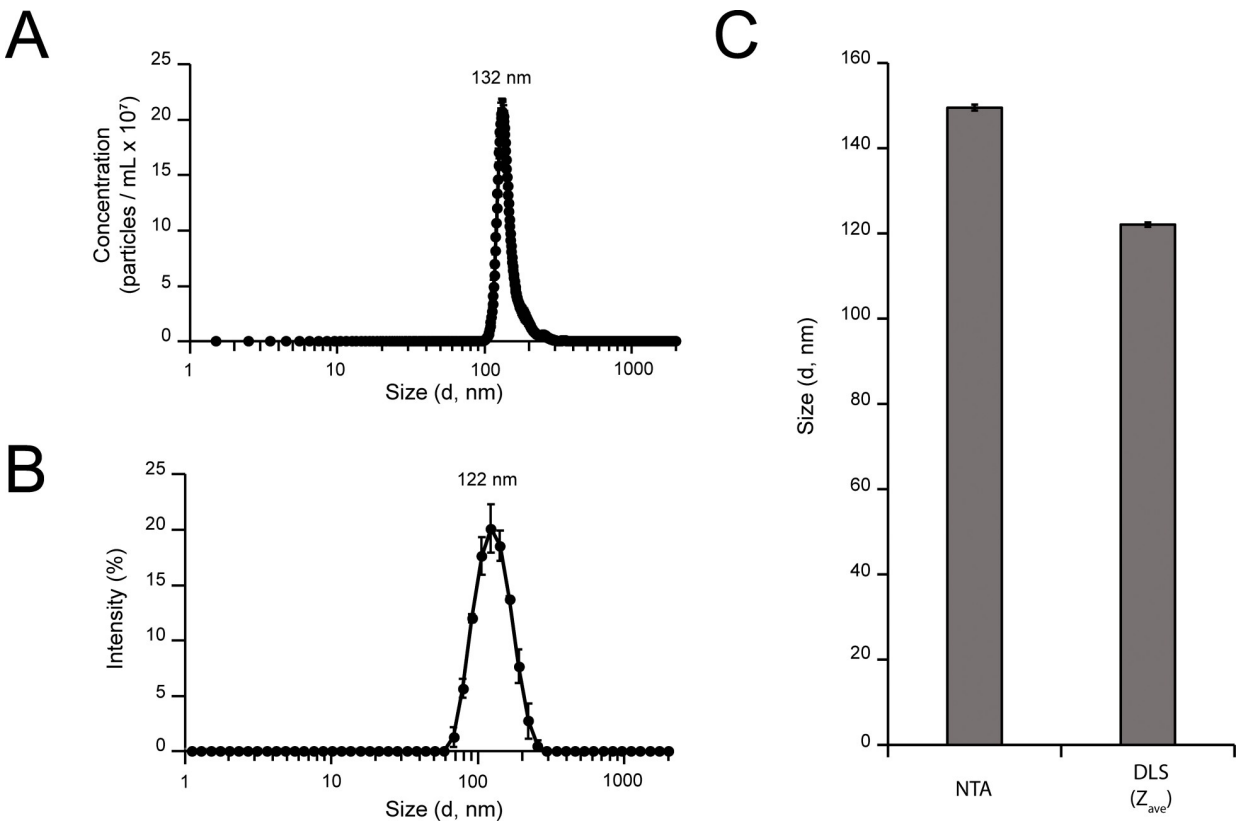

Fig 6. Higher-throughput sizing of purified MCPs using DLS. Sizing MCPs in solution via light scattering techniques. (A) Particle size distributions measured via Nanosight, and (B) Zeta Sizer. (C) Comparison of average diameters measured via NTA and DLS. Error bars represent the standard deviation of the three measured samples.

https://doi.org/10.1371/journal.pone.0226395.g006

based size measurements. Sizing analyses were performed on MCPs in solution (Fig 6), and particle size distributions (PSDs) were acquired (Fig 6A and 6B). When analyzed via Nanosight, the resulting distribution peak reached a maximum at 132 nm (Fig 6A). When analyzed via Zeta Sizer, the calculated distribution reached an intensity maximum at 122 nm (Fig 6B). Generally, the particle size distribution peak obtained via Nanosight was narrower than in the Zeta Sizer analysis. The average diameter measured by NTA was 149.5 ± 0.7 nm, which was larger than the 122.04 ± 0.5 nm measured by the Zeta Sizer (Fig 6C). The disparity in mean diameter comes from large aggregates observed in the NTA experiment (S3 Fig). To directly compare the sizing of Nanosight and Zeta Sizer, we consider differences between the mode diameter of Nanosight and the mean diameter (Z_{ave}) of the Zeta Sizer to be the most accurate comparison. The mode diameter of 130.7 ± 1.0 nm is slightly higher than the measured 122.04 ± 0.5 nm observed in Zeta Sizer measurements. Finally, the polydispersity index (PDI), a metric of the broadness of the measured size distribution, calculated via Zeta Sizer was 0.045 ± 0.001. PDI, calculated directly from the DLS correlation data, is dimensionless and scaled such that a value of ~0.05 represents a highly monodisperse sample. We attribute discrepancies in diameter measurements to differences between the measurement techniques and their respective calculations of particle diameter. The full experiment report obtained for NTA measurements is shown in S3 Fig.

To further assess the stability of DLS sizing measurements over an order of magnitude of concentrations of MCPs, we compared size measurements at 50 μg/mL and 500 μg/mL MCPs

using Zeta Sizer (S4 Fig). Importantly, the raw correlation data obtained at 50 μg/mL and 500 μg/mL were in good agreement; the resulting Z_{ave} values calculated were 121.1 ± 0.32 nm and 122.0 ± 0.51 nm, respectively (S4 Fig). Polydispersity indices obtained for MCPs at 50 μg/mL and 500 μg/mL were 0.069 ± 0.001 and 0.045 ± 0.001, respectively, indicating a high degree of uniformity of MCPs (S4 Fig). Full intensity, number, and volume PSDs for DLS measurements are presented in S4 Fig. As expected, we observed similar PSDs for measurements collected at 50 μg/mL and 500 μg/mL MCPs. Intensity PSDs displayed maximum intensities at ~122 nm. Number and volume PSDs displayed maxima near ~90 nm, and were left-shifted with respect to the intensity PSDs. Slight shifting of the PSDs between intensity, number, and volume distributions is attributable to differences in the treatment of correlation data, with the intensity PSD representing the actual particle size most accurately. The consistency and stability of DLS measurements over an order of magnitude of concentration indicate that Zeta Sizer is a suitable technique for analysis of MCPs over a range of concentrations. Notably, the diameters obtained by Zeta Sizer appear more similar to the results obtained by SEM or TEM samples treated with HMDS but are 12–13% smaller than MCPs observed by cryo TEM. However, Nanosight results appeared most similar to those obtained by cryo TEM (132 nm vs. 138 nm).

Conclusion

Our results suggest that the technique used to visualize and measure MCPs can alter how we interpret our experimental results. This is especially important when comparing results across studies which used different techniques to assess their results. Our hope is that this study can provide a guideline for the appropriate use of each of the many available techniques used in the field to assess MCPs (Table 1). Specifically, TEM of purified MCPs is most appropriate for rapidly checking MCP shape and morphology. For more in-depth analyses of the size and morphology of MCPs, cryo-EM, SEM, or a modified form of TEM that dehydrates the sample in a high vapor-pressure solvent may be appropriate. If researchers are primarily interested in the size distribution of a population of MCPs, DLS can be used to quickly provide insight. TEM of ultra-thin sections is most appropriate in situations which the *in vivo* MCP distribution or morphology are under investigation. Our results can be used to contextualize and compare results across different studies by providing approximate percent changes in apparent size for each technique.

Supporting information

S1 Table. Reported sizes of MCPs. The reported size range for MCPs, the work in which the size was reported, the system being analyzed (Propanediol utilization (Pdu), Ethanolamine utilization (Eut), Carboxysome (Carb)), and the technique used for the analysis (TEM of ultra-thin sections (TEM UTS), TEM of purified MCPs (TEM Pur)).
(TIF)

S1 Fig. Coomassie-stained gel of three biological replicates used for EM images. Lanes: (i) molecular weight standard, (ii-iv) replicates of purified Pdu MCPs.
(TIF)

S2 Fig. Diagram of a sectioned sphere. Diagram showing the parameters used in the calculation of the average diameter by ultra-thin sectioning. D_{actual} is the true diameter of the sphere, r is the variable describing the distance from the center of the sphere, θ is the azimuthal angle, Φ is the zenith angle, and $d(r)$ is the diameter of an arbitrary circular slice in the sphere at distance r from the center.
(TIF)

S3 Fig. Full Nanosight/NTA analysis report used in this study.
(TIF)

S4 Fig. DLS analysis of MCPs at 50 μg/mL and 500 μg/mL. Raw correlation data (A), calculated Zave (B), and polydispersity indices (PDI) (C) of MCPs. Intensity (D), number (E), volume (F) particle size distributions of MCPs.
(TIF)

S1 File. Raw sizing data from images.
(CSV)

S2 File. Calculation of average measured diameter of a sphere.
(PDF)

S3 File. Raw sizing data from Zeta Sizer.
(XLSX)

S4 File. Raw sizing data from Nanosight.
(XLSX)

S5 File. Raw, uncropped SDS-PAGE gels of purified MCP samples.
(PDF)

Acknowledgments

The authors would like to thank Robert Colby, Mark Heinnickel, and Giovanni Pilloni for their helpful thoughts on additional methods to include in this work, and members of the Tullman-Ercek lab, especially Dr. Svetlana Ikonomova, for helpful comments during the preparation of this manuscript. We also thank Dr. Ben Long of the Australian National University for the useful suggestions regarding the basis of our ultra-thin section observations.

Author Contributions

Conceptualization: Nolan W. Kennedy, Jasmine M. Hershewe, Taylor M. Nichols, Eric W. Roth, Charlene D. Wilke, Carolyn E. Mills, Michael C. Jewett, Danielle Tullman-Ercek.

Data curation: Nolan W. Kennedy, Jasmine M. Hershewe, Taylor M. Nichols, Eric W. Roth, Charlene D. Wilke.

Formal analysis: Nolan W. Kennedy, Jasmine M. Hershewe, Taylor M. Nichols, Eric W. Roth, Charlene D. Wilke, Carolyn E. Mills, Danielle Tullman-Ercek.

Funding acquisition: Michael C. Jewett, Danielle Tullman-Ercek.

Investigation: Nolan W. Kennedy, Jasmine M. Hershewe, Taylor M. Nichols, Eric W. Roth, Charlene D. Wilke, Carolyn E. Mills, Danielle Tullman-Ercek.

Methodology: Nolan W. Kennedy, Jasmine M. Hershewe, Taylor M. Nichols, Eric W. Roth, Charlene D. Wilke, Danielle Tullman-Ercek.

Project administration: Nolan W. Kennedy, Michael C. Jewett, Danielle Tullman-Ercek.

Resources: Michael C. Jewett.

Supervision: Michael C. Jewett, Danielle Tullman-Ercek.

Visualization: Nolan W. Kennedy.

Writing – original draft: Nolan W. Kennedy.

Writing – review & editing: Nolan W. Kennedy, Jasmine M. Hershewe, Taylor M. Nichols, Eric W. Roth, Charlene D. Wilke, Carolyn E. Mills, Michael C. Jewett, Danielle Tullman-Ercek.

References

1. Begley CG, Ioannidis JPA. Reproducibility in Science: Improving the Standard for Basic and Preclinical Research. Circ Res. 2015 Jan 2; 116(1):116–26. https://doi.org/10.1161/CIRCRESAHA.114.303819 PMID: 25552691
2. Goodman SN, Fanelli D, Ioannidis JPA. What does research reproducibility mean? Sci Transl Med. 2016 Jun 1; 8(341):341ps12–341ps12. https://doi.org/10.1126/scitranslmed.aaf5027 PMID: 27252173
3. Allison DB, Brown AW, George BJ, Kaiser KA. Reproducibility: A tragedy of errors. Nature. 2016 Feb; 530(7588):27–9. https://doi.org/10.1038/530027a PMID: 26842041
4. Bobik TA, Lehman BP, Yeates TO. Bacterial microcompartments: widespread prokaryotic organelles for isolation and optimization of metabolic pathways. Mol Microbiol. 2015 Oct; 98(2):193–207. https://doi.org/10.1111/mmi.13117 PMID: 26148529
5. Held M, Quin MB, Schmidt-Dannert C. Eut Bacterial Microcompartments: Insights into Their Function, Structure, and Bioengineering Applications. J Mol Microbiol Biotechnol. 2013; 23(4–5):308–20. https://doi.org/10.1159/000351343 PMID: 23920494
6. Rae BD, Long BM, Badger MR, Price GD. Functions, Compositions, and Evolution of the Two Types of Carboxysomes: Polyhedral Microcompartments That Facilitate CO2 Fixation in Cyanobacteria and Some Proteobacteria. Microbiol Mol Biol Rev. 2013 Sep 1; 77(3):357–79. https://doi.org/10.1128/MMBR.00061-12 PMID: 24006469
7. Drews G, Niklowitz W. [Cytology of Cyanophycea. II. Centroplasm and granular inclusions of Phormidium uncinatum]. Arch Mikrobiol. 1956; 24(2):147–62. PMID: 13327992
8. Shively JM, Decker GL, Greenawalt JW. Comparative Ultrastructure of the Thiobacilli. J Bacteriol. 1970 Feb; 101(2):618–27. PMID: 5413830
9. Shively JM, Ball F, Brown DH, Saunders RE. Functional organelles in prokaryotes: polyhedral inclusions (carboxysomes) of Thiobacillus neapolitanus. Science. 1973 Nov 9; 182(4112):584–6. https://doi.org/10.1126/science.182.4112.584 PMID: 4355679
10. Dou Z, Heinhorst S, Williams EB, Murin CD, Shively JM, Cannon GC. CO $_2$ Fixation Kinetics of *Halothiobacillus neapolitanus* Mutant Carboxysomes Lacking Carbonic Anhydrase Suggest the Shell Acts as a Diffusional Barrier for CO $_2$. J Biol Chem. 2008 Apr 18; 283(16):10377–84. https://doi.org/10.1074/jbc.M709285200 PMID: 18258595
11. Price GD, Badger MR. Expression of Human Carbonic Anhydrase in the Cyanobacterium Synechococcus PCC7942 Creates a High CO2-Requiring Phenotype 1. Plant Physiol. 1989 Oct; 91(2):505–13. https://doi.org/10.1104/pp.91.2.505 PMID: 16667062
12. Mangan NM, Brenner MP. Systems analysis of the CO2 concentrating mechanism in cyanobacteria. eLife. 2014 Apr 29; 3:e02043.
13. Chowdhury C, Sinha S, Chun S, Yeates TO, Bobik TA. Diverse Bacterial Microcompartment Organelles. Microbiol Mol Biol Rev MMBR. 2014 Sep; 78(3):438–68. https://doi.org/10.1128/MMBR.00009-14 PMID: 25184561
14. Axen SD, Erbilgin O, Kerfeld CA. A Taxonomy of Bacterial Microcompartment Loci Constructed by a Novel Scoring Method. Tanaka MM, editor. PLoS Comput Biol. 2014 Oct 23; 10(10):e1003898. https://doi.org/10.1371/journal.pcbi.1003898 PMID: 25340524
15. Jorda J, Lopez D, Wheatley NM, Yeates TO. Using comparative genomics to uncover new kinds of protein-based metabolic organelles in bacteria. Protein Sci. 2013 Feb; 22(2):179–95. https://doi.org/10.1002/pro.2196 PMID: 23188745
16. Bobik T, Havemann G, Busch R, Williams D, Aldrich H. The propanediol utilization (pdu) operon of Salmonella enterica serovar typhimurium LT2 includes genes necessary for formation of polyhedral organelles involved in coenzyme B-12-dependent 1,2-propanediol degradation. J Bacteriol. 1999 Oct; 181(19):5967–75. PMID: 10498708
17. Brinsmade SR, Paldon T, Escalante-Semerena JC. Minimal Functions and Physiological Conditions Required for Growth of Salmonella enterica on Ethanolamine in the Absence of the Metabolosome. J Bacteriol. 2005 Nov 15; 187(23):8039–46. https://doi.org/10.1128/JB.187.23.8039-8046.2005 PMID: 16291677

18. Chen P, Andersson DI, Roth JR. The control region of the pdu/cob regulon in Salmonella typhimurium. J Bacteriol. 1994 Sep; 176(17):5474–82. https://doi.org/10.1128/jb.176.17.5474-5482.1994 PMID: 8071226

19. Stojiljkovic I, Bäumler AJ, Heffron F. Ethanolamine utilization in Salmonella typhimurium: nucleotide sequence, protein expression, and mutational analysis of the cchA cchB eutE eutJ eutG eutH gene cluster. J Bacteriol. 1995; 177(5):1357–1366. https://doi.org/10.1128/jb.177.5.1357-1366.1995 PMID: 7868611

20. Parsons JB, Dinesh SD, Deery E, Leech HK, Brindley AA, Heldt D, et al. Biochemical and Structural Insights into Bacterial Organelle Form and Biogenesis. J Biol Chem. 2008 May 23; 283(21):14366–75. https://doi.org/10.1074/jbc.M709214200 PMID: 18332146

21. Havemann GD, Bobik TA. Protein Content of Polyhedral Organelles Involved in Coenzyme B12-Dependent Degradation of 1,2-Propanediol in Salmonella enterica Serovar Typhimurium LT2. J Bacteriol. 2003 Sep; 185(17):5086–95. https://doi.org/10.1128/JB.185.17.5086-5095.2003 PMID: 12923081

22. Schmid MF, Paredes AM, Khant HA, Soyer F, Aldrich HC, Chiu W, et al. Structure of Halothiobacillus neapolitanus carboxysomes by cryo-electron tomography. J Mol Biol. 2006 Dec 1; 364(3):526–35. https://doi.org/10.1016/j.jmb.2006.09.024 PMID: 17028023

23. Choudhary S, Quin MB, Sanders MA, Johnson ET, Schmidt-Dannert C. Engineered protein nano-compartments for targeted enzyme localization. PloS One. 2012; 7(3):e33342. https://doi.org/10.1371/journal.pone.0033342 PMID: 22428024

24. Slininger Lee MF, Jakobson CM, Tullman-Ercek D. Evidence for Improved Encapsulated Pathway Behavior in a Bacterial Microcompartment through Shell Protein Engineering. ACS Synth Biol. 2017 Oct 20; 6(10):1880–91. https://doi.org/10.1021/acssynbio.7b00042 PMID: 28585808

25. Lawrence AD, Frank S, Newnham S, Lee MJ, Brown IR, Xue W-F, et al. Solution Structure of a Bacterial Microcompartment Targeting Peptide and Its Application in the Construction of an Ethanol Bioreactor. ACS Synth Biol. 2014 Jul; 3(7):454–65. https://doi.org/10.1021/sb4001118 PMID: 24933391

26. Lee MJ, Mantell J, Brown IR, Fletcher JM, Verkade P, Pickersgill RW, et al. De novo targeting to the cytoplasmic and luminal side of bacterial microcompartments. Nat Commun. 2018 Aug 24; 9(1):1–11. https://doi.org/10.1038/s41467-017-02088-w

27. Slininger Lee M, Tullman-Ercek D. Practical considerations for the encapsulation of multi-enzyme cargos within the bacterial microcompartment for metabolic engineering. Curr Opin Syst Biol. 2017 Oct 1; 5:16–22.

28. Dueber JE, Wu GC, Malmirchegini GR, Moon TS, Petzold CJ, Ullal AV, et al. Synthetic protein scaffolds provide modular control over metabolic flux. Nat Biotechnol. 2009 Aug; 27(8):753–9. https://doi.org/10.1038/nbt.1557 PMID: 19648908

29. Sampson EM, Bobik TA. Microcompartments for B12-Dependent 1,2-Propanediol Degradation Provide Protection from DNA and Cellular Damage by a Reactive Metabolic Intermediate. J Bacteriol. 2008 Apr 15; 190(8):2966–71. https://doi.org/10.1128/JB.01925-07 PMID: 18296526

30. Jakobson CM, Tullman-Ercek D, Slininger MF, Mangan NM. A systems-level model reveals that 1, 2-Propanediol utilization microcompartments enhance pathway flux through intermediate sequestration. PLoS Comput Biol. 2017; 13(5):e1005525. https://doi.org/10.1371/journal.pcbi.1005525 PMID: 28475631

31. Cheng S, Fan C, Sinha S, Bobik TA. The PduQ Enzyme Is an Alcohol Dehydrogenase Used to Recycle NAD+ Internally within the Pdu Microcompartment of Salmonella enterica. Hensel M, editor. PLoS ONE. 2012 Oct 15; 7(10):e47144. https://doi.org/10.1371/journal.pone.0047144 PMID: 23077559

32. Chowdhury C, Chun S, Pang A, Sawaya MR, Sinha S, Yeates TO, et al. Selective molecular transport through the protein shell of a bacterial microcompartment organelle. Proc Natl Acad Sci. 2015 Mar 10; 112(10):2990–5. https://doi.org/10.1073/pnas.1423672112 PMID: 25713376

33. Uddin I, Frank S, Warren MJ, Pickersgill RW. A Generic Self-Assembly Process in Microcompartments and Synthetic Protein Nanotubes. Small. 0(0):1704020.

34. Lee MJ, Mantell J, Hodgson L, Alibhai D, Fletcher JM, Brown IR, et al. Engineered synthetic scaffolds for organizing proteins within the bacterial cytoplasm. Nat Chem Biol. 2017 Dec 11; 14(2):142–7. https://doi.org/10.1038/nchembio.2535 PMID: 29227472

35. Huber I, Palmer DJ, Ludwig KN, Brown IR, Warren MJ, Frunzke J. Construction of Recombinant Pdu Metabolosome Shells for Small Molecule Production in *Corynebacterium glutamicum*. ACS Synth Biol. 2017 Nov 17; 6(11):2145–56. https://doi.org/10.1021/acssynbio.7b00167 PMID: 28826205

36. Cheng S, Sinha S, Fan C, Liu Y, Bobik TA. Genetic analysis of the protein shell of the microcompartments involved in coenzyme B12-dependent 1, 2-propanediol degradation by Salmonella. J Bacteriol. 2011; 193(6):1385–1392. https://doi.org/10.1128/JB.01473-10 PMID: 21239588

37. Pang A, Frank S, Brown I, Warren MJ, Pickersgill RW. Structural Insights into Higher Order Assembly and Function of the Bacterial Microcompartment Protein PduA. J Biol Chem. 2014 Aug 8; 289 (32):22377–84. https://doi.org/10.1074/jbc.M114.569285 PMID: 24873823

38. Jakobson CM, Kim EY, Slininger MF, Chien A, Tullman-Ercek D. Localization of Proteins to the 1,2-Propanediol Utilization Microcompartment by Non-native Signal Sequences Is Mediated by a Common Hydrophobic Motif. J Biol Chem. 2015 Oct 2; 290(40):24519–33. https://doi.org/10.1074/jbc.M115.651919 PMID: 26283792

39. Nichols TM, Kennedy NW, Tullman-Ercek D. Cargo encapsulation in bacterial microcompartments: Methods and analysis. Methods Enzymol. 2019; 617:155–86. https://doi.org/10.1016/bs.mie.2018.12.009 PMID: 30784401

40. Sinha S, Bobik TA. The PduM protein is a structural component of the microcompartments involved in coenzyme 3 B12-dependent 1,2-propanediol degradation by Salmonella. 2012;

41. Kim EY, Slininger MF, Tullman-Ercek D. The effects of time, temperature, and pH on the stability of PDU bacterial microcompartments. Protein Sci. 2014 Oct 1; 23(10):1434–41. https://doi.org/10.1002/pro.2527 PMID: 25053115

42. Schneider CA, Rasband WS, Eliceiri KW. NIH Image to ImageJ: 25 years of image analysis. Nat Methods. 2012 Jul; 9(7):671–5. https://doi.org/10.1038/nmeth.2089 PMID: 22930834

43. Kerfeld CA. Protein Structures Forming the Shell of Primitive Bacterial Organelles. Science. 2005 Aug 5; 309(5736):936–8. https://doi.org/10.1126/science.1113397 PMID: 16081736

44. Tanaka S, Kerfeld CA, Sawaya MR, Cai F, Heinhorst S, Cannon GC, et al. Atomic-Level Models of the Bacterial Carboxysome Shell. Science. 2008 Feb 22; 319(5866):1083–6. https://doi.org/10.1126/science.1151458 PMID: 18292340

45. Cai F, Menon BB, Cannon GC, Curry KJ, Shively JM, Heinhorst S. The Pentameric Vertex Proteins Are Necessary for the Icosahedral Carboxysome Shell to Function as a CO2 Leakage Barrier. PLOS ONE. 2009 Oct 21; 4(10):e7521. https://doi.org/10.1371/journal.pone.0007521 PMID: 19844578

46. Bonacci W, Teng PK, Afonso B, Niederholtmeyer H, Grob P, Silver PA, et al. Modularity of a carbon-fixing protein organelle. Proc Natl Acad Sci. 2012 Jan 10; 109(2):478–83. https://doi.org/10.1073/pnas.1108557109 PMID: 22184212

47. Kim EY, Tullman-Ercek D. A rapid flow cytometry assay for the relative quantification of protein encapsulation into bacterial microcompartments. Biotechnol J. 2014 Mar 1; 9(3):348–54. https://doi.org/10.1002/biot.201300391 PMID: 24323373

48. Lassila JK, Bernstein SL, Kinney JN, Axen SD, Kerfeld CA. Assembly of Robust Bacterial Microcompartment Shells Using Building Blocks from an Organelle of Unknown Function. J Mol Biol. 2014 May; 426(11):2217–28. https://doi.org/10.1016/j.jmb.2014.02.025 PMID: 24631000

49. Chowdhury C, Chun S, Sawaya MR, Yeates TO, Bobik TA. The function of the PduJ microcompartment shell protein is determined by the genomic position of its encoding gene. Mol Microbiol. 2016 Sep; 101 (5):770–83. https://doi.org/10.1111/mmi.13423 PMID: 27561553

50. Quin MB, Perdue SA, Hsu S-Y, Schmidt-Dannert C. Encapsulation of multiple cargo proteins within recombinant Eut nanocompartments. Appl Microbiol Biotechnol. 2016 Nov; 100(21):9187–200. https://doi.org/10.1007/s00253-016-7737-8 PMID: 27450681

51. Lehman BP, Chowdhury C, Bobik TA. The N Terminus of the PduB Protein Binds the Protein Shell of the Pdu Microcompartment to Its Enzymatic Core. Metcalf WW, editor. J Bacteriol. 2017 Apr 15; 199(8): e00785–16. https://doi.org/10.1128/JB.00785-16 PMID: 28138097

52. Hagen AR, Plegaria JS, Sloan N, Ferlez B, Aussignargues C, Burton R, et al. In Vitro Assembly of Diverse Bacterial Microcompartment Shell Architectures. Nano Lett. 2018 Nov 14; 18(11):7030–7. https://doi.org/10.1021/acs.nanolett.8b02991 PMID: 30346795

53. Hagen A, Sutter M, Sloan N, Kerfeld CA. Programmed loading and rapid purification of engineered bacterial microcompartment shells. Nat Commun. 2018 Jul 23; 9(1):1–10. https://doi.org/10.1038/s41467-017-02088-w

54. Nichols TM, Kennedy NW, Tullman-Ercek D. A genomic integration platform for heterologous cargo encapsulation in 1,2-propanediol utilization bacterial microcompartments. Biochem Eng J. 2020 Apr 15; 156:107496.

55. Havemann GD, Sampson EM, Bobik TA. PduA is a shell protein of polyhedral organelles involved in coenzyme B-12-dependent degradation of 1,2-propanediol in Salmonella enterica serovar typhimurium LT2. J Bacteriol. 2002 Mar; 184(5):1253–61. https://doi.org/10.1128/JB.184.5.1253-1261.2002 PMID: 11844753

56. Pitts AC, Tuck LR, Faulds-Pain A, Lewis RJ, Marles-Wright J. Structural Insight into the Clostridium difficile Ethanolamine Utilisation Microcompartment. Driscoll PC, editor. PLoS ONE. 2012 Oct 29; 7(10): e48360. https://doi.org/10.1371/journal.pone.0048360 PMID: 23144756

57. Cai F, Sutter M, Bernstein SL, Kinney JN, Kerfeld C a. Engineering Bacterial Microcompartment Shells: Chimeric Shell Proteins and Chimeric Carboxysome Shells. ACS Synth Biol. 2014 Aug; 4(4):444–53. https://doi.org/10.1021/sb500226j PMID: 25117559

58. Sutter M, Greber B, Aussignargues C, Kerfeld CA. Assembly principles and structure of a 6.5-MDa bacterial microcompartment shell. Science. 2017 Jun 23; 356(6344):1293–7. https://doi.org/10.1126/science.aan3289 PMID: 28642439

59. Cheng S, Liu Y, Crowley CS, Yeates TO, Bobik TA. Bacterial microcompartments: their properties and paradoxes. BioEssays. 2008 Nov; 30(11–12):1084–95. https://doi.org/10.1002/bies.20830 PMID: 18937343